Dual-Mode Ring Resonator Bandpass Filter With Asymmetric Inductive Coupling and Its Miniaturization

Tsu-Wei Lin, Jen-Tsai Kuo, *Senior Member, IEEE*, and Shyh-Jong Chung, *Senior Member, IEEE*

***Abstract*—Dual-mode ring resonator filters are implemented with asymmetric inductive perturbation for creating transmission zeros on both sides of the passband. In analysis, dependence of the resonance modes and the zeros on positions and sizes of both the inductive and capacitive perturbations is investigated. Under certain conditions, the even- and odd-mode frequencies for a capacitively perturbed ring are the same as the odd and even ones, respectively, for a ring with inductive perturbation. Theoretical background is clearly explained how the two transmission zeros are split up from the center frequency. Two dual-mode ring resonator filters are fabricated and measured for demonstration. To obtain a miniaturized circuit area, the 1-λ ring trace is folded into a double-ring or spiral configuration. The inductive perturbation is chosen as the crossover and implemented by a short high-impedance coplanar waveguide interconnection in the ground plane of the microstrip. Measurement results show good agreement with the simulation responses.**

***Index Terms*—Bandpass filter, capacitive coupling, dual-mode, inductive coupling, microstrip, miniaturization, ring resonator.**

I. Introduction

DUAL-MODE ring resonator filters are one of the most widely used bandpass filters in microwave frequencies. It is popular because of its compact size, good frequency selectivity, and ease of design. The earliest work of the dual-mode ring resonator can be traced to 1970s [1]. In the traditional design, the input and output (I/O) ports are separated spatially at 90° and a capacitive patch is placed at the end of the symmetric plane. The purpose of the perturbation patch is to split up the two degenerate modes so that a nonzero bandwidth can be obtained. In addition, transmission zeros can be created on both sides of the passband, leading to a quasi-elliptic function response. The transmission zeros can be predicted by the transmission-line theory [2]. In [3], given that the bandwidth is constant, the attenuation pole frequencies can be controlled by the perturbation size and the angle between the I/O ports. In [4], the self-coupled ring resonator is used to devise a dual-mode filter with multiple transmission zeros.

Reducing circuit size is always important in implementation of microwave integrated circuits. The area of a conventional square ring resonator is $\lambda/4\times\lambda/4$. Several techniques have been developed for shrinking the ring area [5]–[13]. In [5], the conductor trace is folded to form a meander ring. In [6], the periodic stepped-impedance ring is a reduced-size filter. The slow-wave effect is also a good approach for miniaturizing the ring, e.g., [7]. The shunt capacitors in [8] and open radial stubs in [9] attaching to the peripheral of the ring can significantly reduce the circuit area. In [10], the dual-mode ring is periodically loaded with butterfly radial slot cells on the ground plane to achieve size reduction and wide upper rejection band. In [11], three quarters of a 1-λ ring is replaced by a $\lambda/4$ microstrip to coplanar waveguide (CPW) broadside coupled section so that the area is only around 25% of that of a full-length ring. Each of the four sides of the dual-mode ring in [12] is loaded by a stub with cascaded alternative high- and low-impedance sections for circuit miniaturization and suppression of its second harmonic. In [13], the size reduction is accomplished by synthesized microstrip lines in an asymmetric form. Good rejection levels are obtained at the second, third, and fourth harmonics of the passband.

It is shown that if the patch in the symmetric plane is replaced by a cut, i.e., capacitive coupling is changed to inductive [14], the passband will be changed from quasi-elliptic function to a response with two transmission zeros on the real axis of the complex s-plane [15]. In [16], the attenuation pole frequencies for both capacitive and inductive coupling are derived. The perturbations can be placed in the symmetric axis or in an axis orthogonal to the symmetric axis, forming totally four possible configurations. It is worth mentioning that most of the above dual-mode rings have their perturbations symmetric about the I/O ports. There have been few dual-mode ring resonator filters with asymmetric perturbation thus far [17]. It is shown that if the patch or cut perturbation is moved away from the symmetric plane, the two zeros will change frequencies, showing a flexible technique for realizing various passbands, although the passband becomes asymmetric. The perturbation positions in [17], however, are limited to the corners of the hexagonal ring.

In this paper, a dual-mode ring resonator is studied with either capacitive or inductive perturbation at an arbitrary position. The input and output ports can be spatially separated by a non-90° angle. The non-90° I/O separation is useful for simultaneous excitation of multiorder resonance modes in a ring resonator so that dual-mode dual-band [18] and dual-mode triple-band [19]

Manuscript received December 21, 2011; revised May 14, 2012; accepted June 04, 2012. Date of publication July 05, 2012; date of current version August 28, 2012. This work was supported in part by the National Science Council, Taiwan, under Grant NSC 100-2221-E-182-059-MY2, and in part by Chang Gung University under Grant UERPD2A0021.

T.-W. Lin and S.-J. Chung are with the Institute of Communications Engineering, National Chiao Tung University, Hsinchu 300, Taiwan (e-mail: jeffrey5321@gmail.com; sjchung@cm.nctu.edu.tw).

J.-T. Kuo is with the Department of Electronic Engineering, Chang Gung University, Taoyaun 333, Taiwan (e-mail: jtkuo123@mail.cgu.edu.tw).

Color versions of one or more of the figures in this paper are available online at http://ieeexplore.ieee.org.

Digital Object Identifier 10.1109/TMTT.2012.2205936

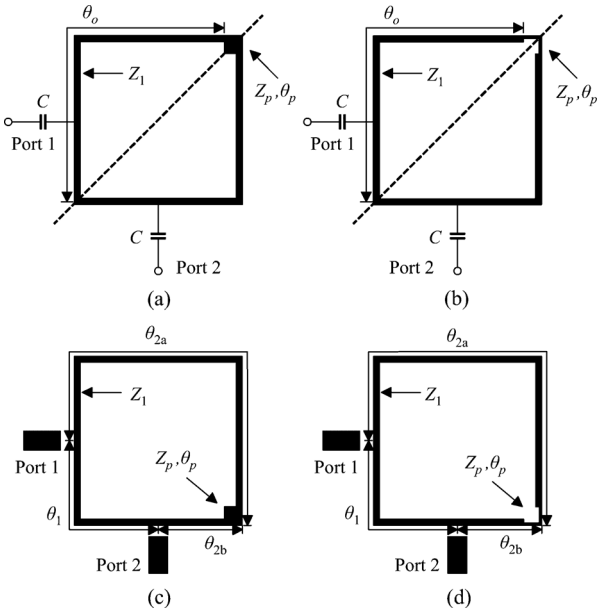

Fig. 1. Dual-mode square ring resonators with a perturbation in symmetric plane. (a) Capacitive. (b) Inductive. Perturbation in an axis perpendicular to the symmetric axis. (c) Capacitive. (d) Inductive. Dashed lines in (a) and (b) show the symmetric planes for analysis of resonance modes.

filters can be realized. In Section II, analysis of transmission poles and zeros of a perturbed ring resonator is conducted and their control is investigated. Based on asymmetric cut perturbation, a dual-mode ring resonator filter with quasi-elliptic passband is demonstrated. In Section III, a reduced-size circuit is implemented by routing half of the ring trace inside the other part. A CPW high-impedance section, incorporating with two conducting vias, is implemented to play the role of the crossover as well as the inductive perturbation, achieving circuit miniaturization. Section IV draws a conclusion.

II. Asymmetric Dual-Mode Ring Resonator and Filter

A. Asymmetric Perturbation

Fig. 1(a) shows the traditional dual-mode ring resonator incorporated with a capacitive perturbation in the symmetric plane, capable of generating a quasi-elliptic function response [2]. The structure in Fig. 1(b) shows no sharp selectivity in the transition bands [14]. In Figs. 1(c) and 1(d), the perturbations are placed in the axis perpendicular to the symmetric axis. These two circuits are simply those in Figs. 1(a) and 1(b) rotated by $+90°$, while keeping the I/O ports fixed. Let the spatial separation between ports 1 and 2 be θ_1, and the traces between the center perturbation and port 1 and port 2 be θ_{2a} and θ_{2b}, respectively. It is known that $\theta_1 + \theta_{2a} + \theta_{2b} = 360°$ at the center frequency, f_o. Obviously, each resonator in Fig. 1 possesses two degenerate modes, and their resonance frequencies f_{p1} and f_{p2} are split up by the perturbation, denoted by characteristic impedance Z_p and electrical length θ_p.

With weak coupling excitations, the transmission responses of Fig. 1(c) and (d) are shown in Fig. 2(a) and (b), respectively. The software package IE3D [20] is employed for the simulation. At center frequency $f_o = 2.45$ GHz, $\theta_1 = 90°$, and the perturbation is allocated at $\theta_{2b} = 0°$, $45°$, $90°$, and $135°$. For the capacitive perturbation in Fig. 2(a), the response for $\theta_{2b} = 135°$ is the result of the traditional ring configuration in Fig. 1(a). When the perturbation is placed at $\theta_{2b} = 45°$, there is no sharp skirt response near the center frequency [14]. Note that when $\theta_{2b} = 0°$ and $90°$, the two peaks have very different magnitudes, and the bandpass response will be difficult to synthesize, due to the destruction of the zero. For the inductive perturbation in Fig. 2(b), on the other hand, the response suitable for synthesis of a quasi-elliptic passband is $\theta_{2b} = 45°$. When the inductive segment is allocated at $\theta_{2b} = 135°$, there is no transmission dip.

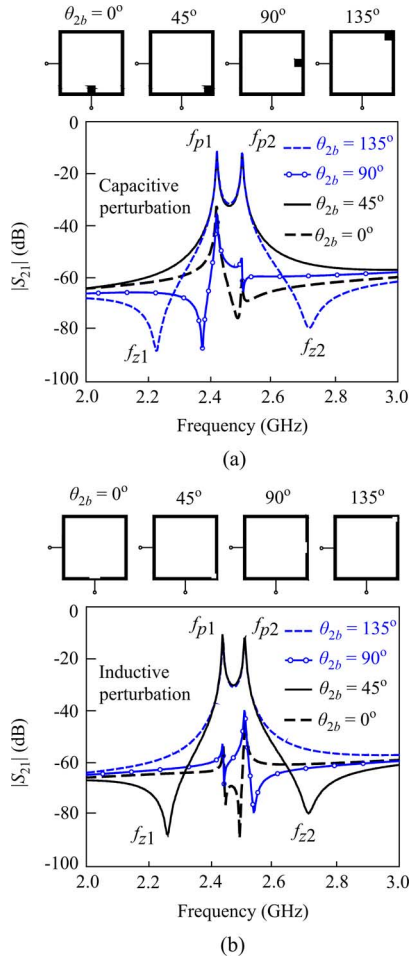

Fig. 2. Transmission responses of Fig. 1(c) and (d) with $\theta_1 = 90°$, $\theta_p = 10°$, $Z_1 = 75\ \Omega$ when $\theta_{2b} = 0°$, $45°$, $90°$, $135°$. (a) Capacitive perturbation, $Z_p = 42.5\ \Omega$. (b) Inductive perturbation, $Z_p = 117.8\ \Omega$.

B. Spacing Between Input and Output Ports

Figs. 3 and 4 investigate the behavior of the zeros when the I/O separation $\theta_1 = 60°$ and $120°$, respectively. In Fig. 3, the perturbation is placed at $\theta_{2b} = 0°$, $50°$, $100°$, and $150°$. Compared with the results in Fig. 2, both f_{z1} and f_{z2} shift to lower frequencies. In Fig. 3(a), when $\theta_{2b} = 50°$, both of them are in the lower stopband, showing a flexible way of zero control. When $\theta_{2b} = 100°$, f_{z2} is between the two transmission poles so it is not suitable for passband synthesis. When $\theta_{2b} = 150°$, the two zeros are on the different sides of the passband, and this circuit is more suitable for passband synthesis than that with $\theta_{2b} = 0°$ since f_{z2} of the latter is very close to f_{p2}. For the in-

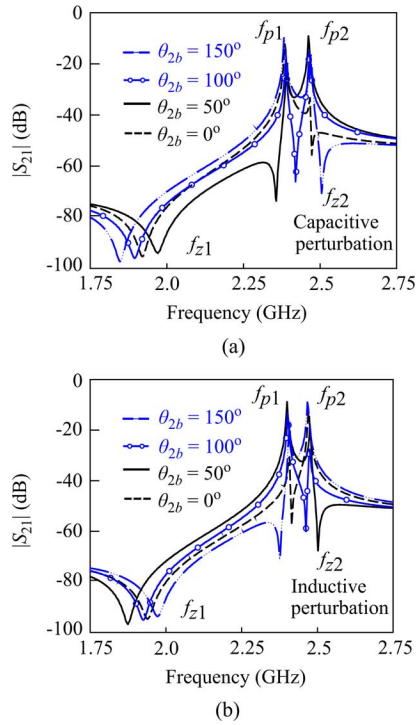

Fig. 3. Transmission responses with $\theta_1 = 60°$, $\theta_p = 10°$ and $Z_1 = 75\ \Omega$ when $\theta_{2b} = 0°, 50°, 100°$, and $150°$. (a) Capacitive perturbation in Fig. 1(c), $Z_p = 42.5\ \Omega$. (b) Inductive perturbation in Fig. 1(d), $Z_p = 117.8\ \Omega$.

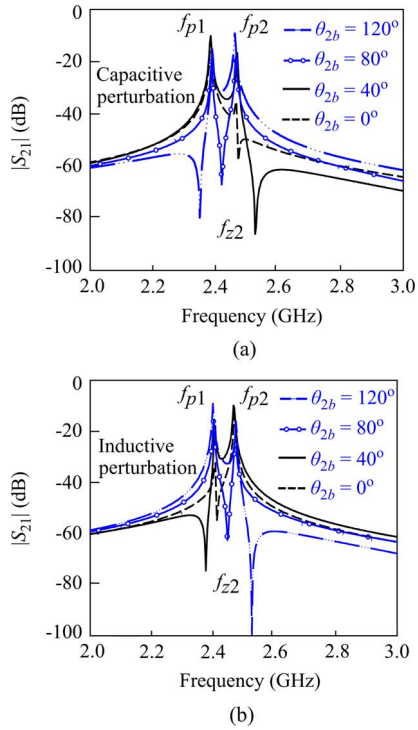

Fig. 4. Transmission responses with $\theta_1 = 120°$, $\theta_p = 10°$, and $Z_1 = 75\ \Omega$ when $\theta_{2b} = 0°, 40°, 80°, 120°$. (a) Capacitive perturbation in Fig. 1(c), $Z_p = 42.5\ \Omega$. (b) Inductive perturbation in Fig. 1(d), $Z_p = 117.8\ \Omega$.

ductive perturbations in Fig. 3(b), the responses for $\theta_{2b} = 0°$, $50°$, $100°$, and $150°$ are similar to those with $\theta_{2b} = 100°$, $150°$, $0°$, and $50°$, respectively, in Fig. 3(a).

In Fig. 4, the I/O separation is $\theta_1 = 120°$, and the perturbation is placed at $\theta_{2b} = 0°$, $40°$, $80°$, and $120°$. It is interesting that only one transmission zero can be observed. For the capacitive perturbation in Fig. 4(a), the zero is on the upper and lower sides of the passband when $\theta_{2b} = 40°$ and $120°$, respectively, while in Fig. 4(b) with inductive perturbation, the zeros on the upper and lower sides are resulted from $\theta_{2b} = 120°$ and $40°$, respectively. For both perturbation types, the responses show that a flat passband supported by f_{p1} and f_{p2} will be difficult to build up by using $\theta_{2b} = 0°$ and $80°$.

C. Transmission Poles and Zeros

Theoretically, the transmission poles of the perturbed rings in Fig. 1 are independent of the excitations. Thus, the resonance frequencies of the rings in Fig. 1(c) and (d) will be the same as those in Fig. 1(a) and (b), respectively. It can be shown that the resonance conditions are

$$\tan\left(\frac{\theta_p}{2}\right) + y_p \tan\theta_o = 0 \quad \text{(odd mode)} \tag{1}$$

$$z_p \tan\theta_o + \tan\left(\frac{\theta_p}{2}\right) = 0 \quad \text{(even mode)} \tag{2}$$

where $\theta_o = \theta_{2a} + \theta_{2b} + \theta_1$ and $y_p = Z_1/Z_p \equiv z_p^{-1}$. The perturbation is of capacitive and inductive type when $z_p < 1$ and $z_p > 1$, respectively. In comparison of (2) and (1), if

$$Z_{p\text{-cap}} \times Z_{p\text{-ind}} = Z_1^2 \tag{3}$$

holds, then the even- and odd-mode frequencies of the capacitive perturbation are the same as the odd- and even-mode frequencies of the inductive cut.

The zero frequencies of the ring resonator filter will depend on the positions of the input and output. For both Fig. 1(c) and (d), the transmission zeros can be obtained by enforcing the total forward transmission admittance of the two signal paths shown in Fig. 5 to zero [2]

$$\sin\theta_1 + \sin(\theta_{2a}+\theta_{2b}) - [(1-z_p)\cos\theta_{2a}\cos\theta_{2b} + (y_p-1)\sin\theta_{2a}\sin\theta_{2b}]\sin\theta_p = 0. \tag{4}$$

It can be rewritten as

$$a + \sin\theta_p(\beta+\delta) = 0 \tag{5a}$$

$$\alpha = 4\sin\left(\pi\frac{f}{f_o}\right)\cos\left(\frac{\theta_{2a}+\theta_{2b}-\theta_1}{2}\right) \tag{5b}$$

$$\beta = (z_p + y_p - 2)\cos(\theta_{2a}+\theta_{2b}-\theta_p) \tag{5c}$$

$$\delta = (z_p - y_p)\cos(\theta_{2a}-\theta_{2b}). \tag{5d}$$

The term α is resulted from the leading two terms in (4) and represents the sum of two admittances when no perturbation exists. When $\theta_1 = 90°$ and $\theta_{2a} + \theta_{2b} = 270°$, the α term indicates a second-order zero at f_o. The effectiveness of the perturbation on split-up or shift of the zeros relies on the second term of (5a). A larger θ_p will lead to a larger split-up. It is known that θ_p is relatively small, and $|\beta| \ll |\delta|$. For example, $y_p = 1.25$, than $z_p + y_p - 2 = 0.05$ and $z_p - y_p = -0.45$. For the traditional capacitively perturbed ring in Fig. 1(a), $\theta_{2a} = \theta_{2b} = 135°$: 1) the

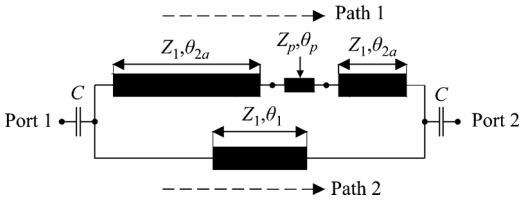

Fig. 5. Two-signal path model for analysis of transmission zeros.

β term in (5) can be neglected 2) when frequencies moves not so far away from f_o, $\alpha > 0$ and its magnitude decreases. Thus, δ must be negative to assure the existence of zeros. This reflects the fact that if a cut is placed here, there will be no zero since $\delta > 0$. When frequency is decreased or increased to the frequencies where $|\alpha| = |\delta|$ is satisfied, transmission zeros occur. On the other hand, for the proposed ring with inductive cut in Fig. 1(d), $\theta_{2a} = 225°$ and $\theta_{2b} = 45°$, and $\theta_{2a} - \theta_{2b} = 180°$. Thus, a patch at this corner will not cause any zero since the cos term in (5d) reverses the sign of δ. Instead, an inductive cut with $z_p - y_p > 0$ is required for the split-up of the two zeros from f_o.

Fig. 6(a) plots variations of the transmission zeros f_{z1} and f_{z2} versus θ_{2b} from $-90°$ to $270°$, based on $Z_1 = 75\ \Omega$, $\theta_p = 10°$, $\theta_{2a} + \theta_{2b} = 270°$, and $\theta_1 = 90°$ at $f_o = 2.45$ GHz. It is noted that when (4) is used for solving the zeros, all electrical lengths are linear functions of frequency. When $Z_p = 90\ \Omega$, two transmission zeros can be found when $0° \le \theta_{2b} \le 90°$ and $180° \le \theta_{2b} \le 270°$, but there is no zero otherwise. The distance between the two zeros varies when θ_{2b} is changed, and the maximal distance occurs around $\theta_{2b} = 45°$ and $225°$. When Z_p is increased to $100\ \Omega$, i.e., more perturbation is employed, the zeros move farther away from the center frequency. When a capacitive patch is applied, e.g., $Z_p = 60\ \Omega$, the two transmission zeros can be found only when $90° \le \theta_{2b} \le 180°$ and $-90° \le \theta_{2b} \le 0°$. Again, when $Z_p = 50$ and $40\ \Omega$, i.e., the amount of perturbation is increased; the distance between the two zeros is increased.

Fig. 6(b) and (c) investigates the changes of f_{z1} and f_{z2} versus θ_{2b} for $\theta_1 = 60°$ and $120°$, respectively. In Fig. 6(b), f_{z1} and f_{z2} variations have smaller ranges than those in Fig. 6(a), and some f_{z2} are close to the center passband. In Fig. 6(c), only one zero (f_{z2}) can be observed, for both capacitive and inductive perturbations. A better understanding for existence of zero, one, or two zeros can be referred to the illustrative description following (5d).

Fig. 7 shows the variations f_{z1} and f_{z2} with respect to the continuous changes of θ_1 from $10°$ to $150°$ by solving (2) for the inductive perturbation with $\theta_{2b} = 45°$. It is interesting that both f_{z1} and f_{z2} have a turning point at around $\theta_1 = 90°$. When θ_1 is decreased from the turning point, f_{z1} decreases while f_{z2} keeps almost flat. Alternatively, when θ_1 is above the turning point, f_{z1} shows only small changes, but f_{z2} increases. The transmission poles can also be plotted along with these zeros [21].

D. Effectiveness of Perturbation Size

As shown in Fig. 6, the frequencies of the two zeros also depend on the size of the perturbation. Let $\theta_1 = 90°$ and $\theta_{2b} = 45°$

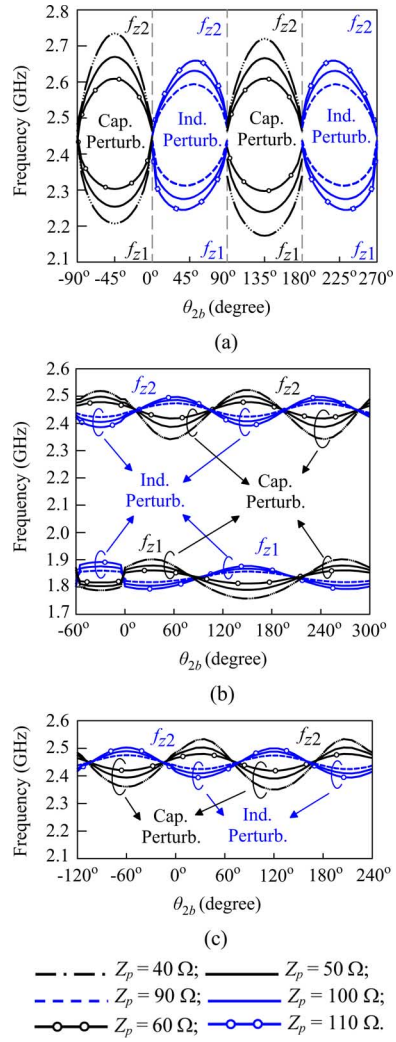

Fig. 6. Transmission zero versus θ_{2b}. $Z_1 = 75\ \Omega$, $\theta_p = 10°$. (a) $\theta_1 = 90°$. (b) $\theta_1 = 60°$. (c) $\theta_1 = 120°$.

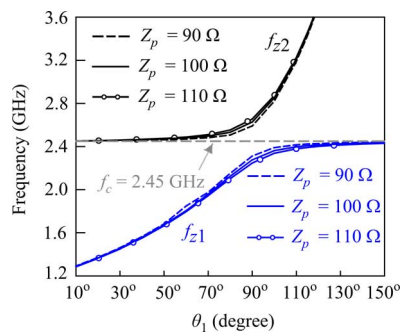

Fig. 7. Transmission zero versus continuous changes of θ_1 for inductive perturbation. $Z_1 = 75\ \Omega$, $\theta_{2b} = 45°$, $\theta_p = 10°$.

at f_o, i.e., the structure shown in Fig. 1(d). The peak frequencies f_{p1} and f_{p2} determine the bandwidth and can be calculated by using the formula in [2] by changing the type of perturbation. Fig. 8 compares f_{p1}, f_{p2}, f_{z1}, and f_{z2} obtained by the IE3D with those obtained by the transmission-line theory for various notch sizes. In Fig. 8(a), when W_p is increased, meaning the notch has less inductive, the resonances and zeros get closer to the center frequency f_o. In Fig. 8(b), when the length of the high-impedance section is increased, f_{p1} and f_{z1} move to lower

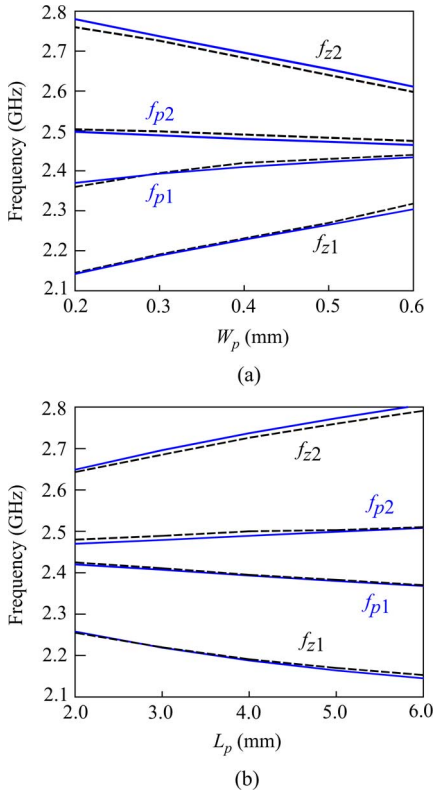

Fig. 8. Variations of transmission zeros and resonant modes versus sizes of the cut. (a) $0.2\ \text{mm} \le W_p \le 0.6\ \text{mm}$, $87\ \Omega \le Z_p \le 136.25\ \Omega$, $L_p = 4.0$ mm, $\theta_p = 15.48°$. (b) $2.0\ \text{mm} \le L_p \le 6.0\ \text{mm}$, $7.74° \le \theta_p \le 23.21°$, $W_p = 0.3$ mm . $\theta_1 = 90°$, $\theta_{2b} = 45°$. Dashed lines: full-wave simulation, solid lines: transmission-line theory.

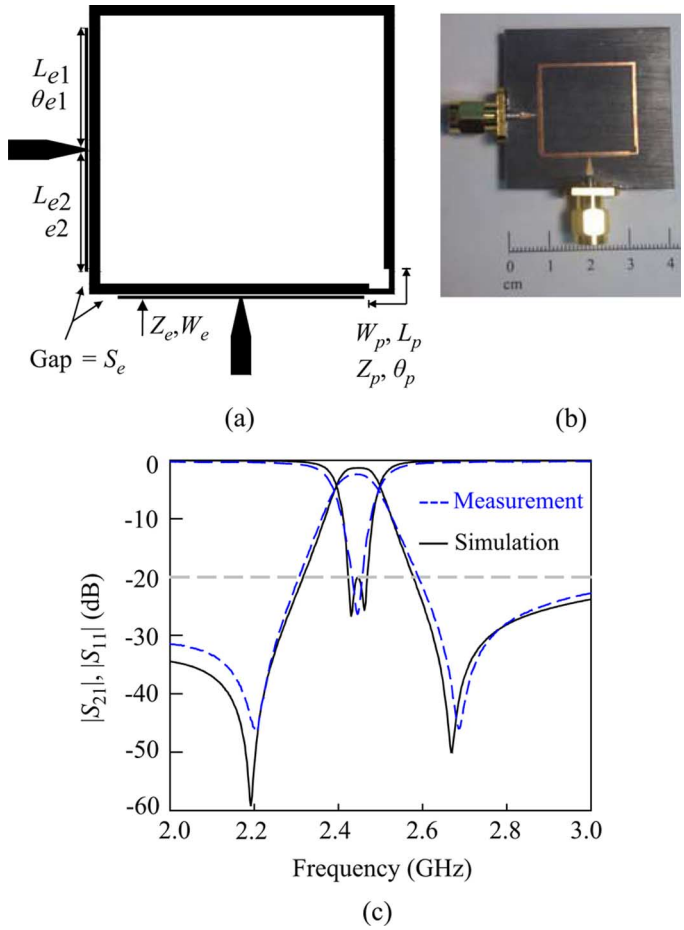

Fig. 9. (a) Layout of the dual-mode ring resonator filter. (b) Photograph of the measured circuit. (c) Simulation and measurement results of the dual-mode ring resonator filter. $W_p = 0.4$ mm, $L_p = 4.0$ mm, $S_e = 0.15$ mm, $W_e = 0.2$ mm, $L_{e1} = 9.9$ mm, $L_{e2} = 9.5$ mm, $W_1 = 0.8$ mm, $L_1 = 22.4$ mm, $L_{2a} = 54.7$ mm, $L_{2b} = 9.98$ mm. Substrate: $\epsilon_r = 2.2$, thickness $= 0.508$ mm.

frequencies, while f_{p2} and f_{z2} shift to higher frequencies, indicating the ring resonator filter will have an increasing bandwidth and a wider space between the two zeros. The results based on the theoretical formulation have good match with those obtained by the full wave simulation. The maximal relative deviation is 0.72%, occurring at the f_{z2} curve.

E. Dual-Mode Ring Resonator Bandpass Filter

The design procedure for the dual-mode ring resonator filter is: 1) determine circuit bandwidth and number and positions of transmission zeros from the plots in Figs. 2–4; 2) choose type of perturbation type, i.e., patch or cut, and its position along the ring peripheral; and 3) choose the excitation angle and the line-to-ring coupling [22] for I/O matching.

The dual-mode ring resonator with asymmetric inductive perturbation can be devised to synthesize a quasi-elliptic function bandpass filter. The circuit layout is shown in Fig. 9(a), and the photograph of the measured circuit in Fig. 9(b). The design parameters include $Z_1 = 75\ \Omega$, $Z_p = 105\ \Omega$, $\theta_p = 15.5°$, $\theta_1 = 90°$, $\theta_{2a} = 222.7°$, and $\theta_{2b} = 47.3°$. Fig. 9(c) shows the simulation and measurement results of Fig. 9(a). It is designed at center frequency $f_o = 2.45$ GHz with a fractional bandwidth $\Delta = 4.45\%$. The substrate has a dielectric constant $\epsilon_r = 2.2$ and thickness $h = 0.508$ mm. At f_o, the measured insertion loss is 2.37 dB, and the return loss is better than 20 dB. The two transmission zeros are at 2.23 and 2.72 GHz. Simulation and measurement results show good agreement.

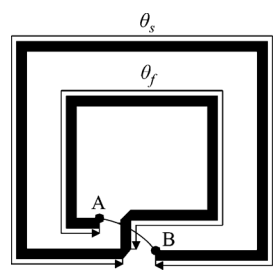

Fig. 10. Double-ring configuration.

III. Circuit Miniaturization

To obtain a compact circuit area, the ring can be folded to a double-ring or spiral configuration, as shown in Fig. 10, where a 3-D structure will be required for connecting points A and B of the inner and outer rings, of which the electrical lengths are θ_f and θ_s, respectively. The 3-D implementation can be a short bonding wire or a short high-impedance section incorporating with two via-holes. Both of them are equivalent to an inductor. Here, for ease of fabrication, the later is chosen. The high-impedance section is made on the ground plane of the microstrip, forming a CPW segment. Such a CPW section plays a different role from that in [11] where a quarter-wave

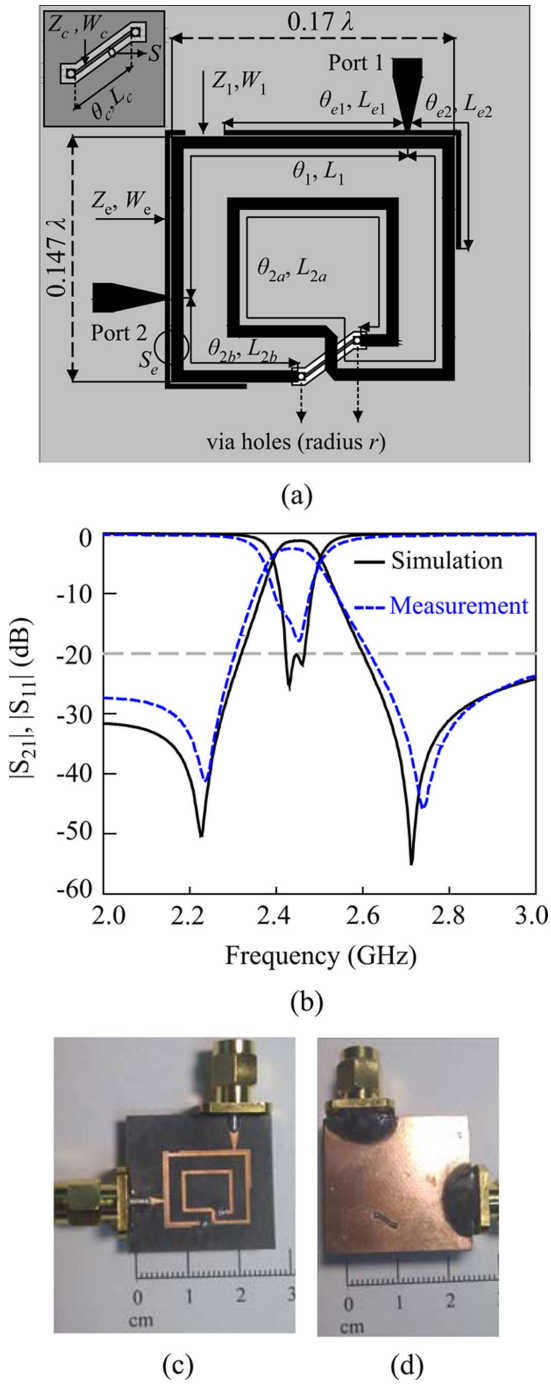

Fig. 11. (a) Layout of miniaturized dual-mode ring resonator filter. (b) Simulated and measured results. Photograph of the measured circuit. (c) Top view. (d) Bottom view. $S = 0.32$ mm, $r = 0.2$ mm, $W_c = 0.15$ mm, $L_c = 3.36$ mm, $S_e = 0.15$ mm, $W_e = 0.2$ mm, $L_{e1} = 10.02$ mm, $L_{e2} = 9.77$ mm, $W_1 = 0.6$ mm, $L_1 = 22.7$ mm, $L_{2a} = 51.8$ mm, $L_{2b} = 10.52$ mm. CPW section: $\epsilon_{reff} = 1.504$, $Z_c = 134.4\ \Omega$, $\theta_c = 12.12°$. Substrate: $\epsilon_r = 2.2$, thickness $= 0.508$ mm.

microstrip-to-CPW broadside coupled line is used to replace a transmission-line section of 270°. For saving the implementation effort, the line-to-ring structure is kept as close as possible to that in Fig. 9(a). Thus, a certain space between the two loops is used for preventing coupling between the adjacent traces. Fig. 11(a) shows the top view of the circuit layout. The top metal in black is used for the microstrip, the bottom metal in gray is for the ground plane, and the CPW high-impedance segment. In design, the coupling between the microstrip and the CPW section is neglected since not only the overlapped area is small, but also both signal traces are nearly perpendicular to each other. The coupling between parallel microstrip ring traces may change the total coupling coefficient, and hence, the filter bandwidth. To eliminate the unwanted coupling, our simulation data suggest that the distance between the parallel traces should keep at least three times the line width. The radius of the two via-holes is r. As a result, the circuit has a size of $0.17\lambda_g \times 0.147\lambda_g$, and its area is about 39.8% of that of a conventional square ring resonator.

Fig. 11(b) compares measurement results with the simulation. The circuit parameters include $\theta_f = 135.5°$, $Z_1 = 87\ \Omega$, $Z_c = 134.4\ \Omega$, $\theta_c = 12.12°$, $\theta_{2a} = 222.6°$, $\theta_{2b} = 47.4°$, $\theta_1 = 90°$ and $f_o = 2.45$ GHz. The equivalent inductance is 1.83 nH. The measured insertion loss at f_o is 2.52 dB, the fractional bandwidth $\Delta = 5.18\%$ and the return loss is better than 15 dB. Two transmission zeros are at 2.235 and 2.74 GHz, respectively. Good agreement between simulation and measurement results can be observed. Fig. 11(c) and (d) shows the photographs of the top and bottom sizes of the measured circuit.

IV. Conclusion

Characteristics of the transmission zeros of dual-mode ring resonator filters with asymmetric and symmetric inductive and capacitive perturbations are investigated for bandpass filter design. Quasi-elliptic function passband can be obtained by placing the inductive perturbation at a position of 90° away from the end of the symmetric axis, where is the capacitive patch location of a traditional dual-mode ring resonator filter. When the product of the characteristic impedances of the patch and cut sections equals square of the characteristic impedance of the uniform trace, the even- and odd-mode frequencies are switched when the perturbation type is exchanged. Variations of the transmission zeros versus I/O port separation θ_1 and perturbation position θ_{2b} are investigated, and design curves plotted. When $\theta_1 = 60°$, the two zeros shift down to lower frequencies for both capacitive and inductive perturbations. The dual-mode ring with inductive cut is folded to a double-ring configuration and the inductive perturbation is implemented by a CPW high-impedance section on the ground plane, leading to the normalized circuit area reduced to 39.8%. Measurement data show good agreement with simulation results.

References

[1] I. Wolff, "Microstrip bandpass filter using degenerate modes of a microstrip ring resonator," *Electron. Lett.*, vol. 8, no. 12, pp. 302–303, Jun. 1972.

[2] M. Matsuo, H. Yabuki, and M. Makimoto, "Dual-mode stepped-impedance ring resonator for bandpass filter applications," *IEEE Trans. Microw. Theory Tech.*, vol. 49, no. 7, pp. 1235–1240, Jul. 2001.

[3] A. C. Kundu and I. Awai, "Control of attenuation pole frequency of a dual-mode microstrip ring resonator bandpass filter," *IEEE Trans. Microw. Theory Tech.*, vol. 49, no. 6, pp. 1113–1117, Jun. 2001.

[4] Y.-H. Jeng, S.-F. Chang, Y.-M. Chen, and Y.-J. Huang, "A novel self-coupled dual-mode ring resonator and its applications to bandpass filter," *IEEE Trans. Microw. Theory Tech.*, vol. 54, no. 5, pp. 2146–2151, May 2006.

[5] J. S. Hong and M. J. Lancaster, "Microstrip bandpass filter using degenerate modes of a novel meander loop resonator," *IEEE Microw. Guided Wave Lett.*, vol. 5, no. 11, pp. 371–372, Nov. 1995.

[6] J.-T. Kuo and C.-Y. Tsai, "Periodic stepped-impedance ring resonator (PSIRR) filter with a miniaturized area and desirable upper stopband characteristics," *IEEE Trans. Microw. Theory Tech.*, vol. 54, no. 3, pp. 1107–1112, Mar. 2006.
[7] A. Görür and C. Karpuz, "Miniature dual-mode microstrip filters," *IEEE Microw. Wireless Comp. Lett.*, vol. 17, no. 1, pp. 37–39, Jun. 2007.
[8] M.-F. Lei and H. Wang, "An analysis of miniaturized dual-mode bandpass filter structure using shunt-capacitance perturbation," *IEEE Trans. Microw. Theory Tech.*, vol. 53, no. 3, pp. 861–867, Mar. 2005.
[9] B. T. Tan, J. J. Yu, S. T. Chew, M.-S. Leong, and B.-L. Ooi, "A miniaturized dual-mode ring bandpass filter with a new perturbation," *IEEE Trans. Microw. Theory Tech.*, vol. 53, no. 1, pp. 343–348, Jan. 2005.
[10] R.-J. Mao, X.-H. Tang, and F. Xiao, "Miniaturized dual-mode ring bandpass filters with patterned ground plane," *IEEE Trans. Microw. Theory Tech.*, vol. 55, no. 7, pp. 1539–1547, Jul. 2007.
[11] Y.-C. Chiou, J.-T. Kuo, and J.-S. Wu, "Miniaturized dual-mode ring resonator bandpass filter with microstrip-to-CPW broadside-coupled structure," *IEEE Microw. Wireless Compon. Lett.*, vol. 18, no. 2, pp. 97–99, Feb. 2008.
[12] J. Wang, J.-L Li , J. Ni, S. Zhao, W. Wu, and D. Fang, "Design of miniaturized microstrip dual-mode filter with source-load coupling," *IEEE Microw. Wireless Compon. Lett.*, vol. 20, no. 6, pp. 319–321, Jun. 2010.
[13] H.-W. Hsu, C.-H. Lai, and T.-G. Ma, "A miniaturized dual-mode ring bandpass filter," *IEEE Microw. Wireless Compon. Lett.*, vol. 20, no. 10, pp. 542–544, Oct. 2010.
[14] A. Görür, "Description of coupling between degenerate modes of a dual-mode microstrip loop resonator using a novel perturbation arrangement and its dual-mode bandpass filter application," *IEEE Trans. Microw. Theory Tech.*, vol. 52, no. 2, pp. 671–677, Feb. 2004.
[15] S. Amari, "Comments on "Description of coupling between degenerate modes of a dual-mode microstrip loop resonator using a novel perturbation arrangement and its dual-mode bandpass filter application," *IEEE Trans. Microw. Theory Tech.*, vol. 52, no. 9, pp. 2190–2192, Sep. 2004.
[16] I. Awai, "General theory of a circular dual-mode resonator and filter," *IEICE Trans. Electron.*, vol. E81-C, no. 11, pp. 1757–1763, Nov. 1998.
[17] R.-J. Mao and X.-H. Tang, "Novel dual-mode bandpass filters using hexagonal loop resonators," *IEEE Trans. Microw. Theory Tech.*, vol. 54, no. 9, pp. 3526–3533, Sep. 2006.
[18] S. Luo, L. Zhu, and S. Sun, "A dual-band ring-resonator bandpass filter based on two pairs of degenerate modes," *IEEE Trans. Microw. Theory Tech.*, vol. 58, no. 12, pp. 3427–3432, Dec. 2010.
[19] S. Luo, L. Zhu, and S. Sun, "Compact dual-mode triple-band bandpass filters using three pairs of degenerate modes in a ring resonator," *IEEE Trans. Microw. Theory Tech.*, vol. 59, no. 5, pp. 1222–1229, May 2011.
[20] IE3D Simulator. Zeland Softw. Inc., Fremont, CA, Jan. 1997.
[21] Y.-C. Chiou, P.-S. Yang, J.-T. Kuo, and C.-Y. Wu, "Transmission zero design graph for dual-mode dual-band filter with periodic stepped-impedance ring resonator," *Progr. Electromagn. Res.*, vol. 108, pp. 23–36, 2010.
[22] L. Zhu and K. Wu, "A joint field/circuit model of line-to-ring coupling structures and its application to the design of microstrip dual-mode filters and ring resonator circuits," *IEEE Trans. Microw. Theory Tech.*, vol. 47, no. 10, pp. 1938–1948, Oct. 1999.

Tsu-Wei Lin was born in Taichung, Taiwan. He received the B.S. degree from National Chung Cheng University, Taiwan, in 2009, the M.S. degree from National Chiao Tung University, Taiwan, in 2010, and is currently working toward the Ph.D. degree from the Institute of Communications Engineering, National Chiao Tung University, Hsinchu, Taiwan.

His research interests include design of planar filters and associated RF modules for microwave applications.

Jen-Tsai Kuo (S'88–M'92–SM'04) received the Ph.D. degree from the Institute of Electronics, National Chiao Tung University (NCTU), Hsinchu, Taiwan, in 1992.

From 1984 to 2010, he was with the Department of Communication Engineering, NCTU. From 1995 to 1996, he was a Visiting Scholar with the Electrical Engineering Department, University of California at Los Angeles (UCLA). He is currently a Professor with the Department of Electronic Engineering, Chang Gung University, Taoyuan, Taiwan. His research interests include analysis and design of microwave integrated circuits and numerical techniques in electromagnetics.

Dr. Kuo is a member of the IEEE MTT-8 Subcommittee (Filters and Passive Components). He is an Editorial Board member for the IEEE TRANSACTIONS ON MICROWAVE THEORY AND TECHNIQUES and the IEEE MICROWAVE AND WIRELESS COMPONENTS LETTERS. He was an associate editor for the IEEE TRANSACTIONS ON MICROWAVE THEORY AND TECHNIQUES (2008–2010). He was a recipient of the Best Paper Award presented at the 2002 National Telecommunication Conference, Taiwan, the 2007 Asia–Pacific Microwave Conference (APMC) Prize, Bangkok, Thailand, and the 2008 APMC Prize, Hong Kong. He was the recipient of the 2006 Taiwan Citation Laureate presented by Thomson Scientific and the 2007 Distinguished Research Award presented by the National Science Council, Taiwan.

Shyh-Jong Chung (M'92–SM'06) was born in Taipei, Taiwan. He received the B.S.E.E. and Ph.D. degrees from National Taiwan University, Taipei, Taiwan, in 1984 and 1988, respectively.

Since 1988, he has been with the Department of Communication Engineering and the Department of Electrical Engineering, National Chiao Tung University (NCTU), Hsinchu, Taiwan, where he is currently a Professor. From 2009 to 2011, he was the Director of the Institute of Communication Engineering, NCTU. From September 1995 to August 1996, he was a Visiting Scholar with the Department of Electrical Engineering, Texas A&M University, College Station. His areas of interest include the design and applications of active and passive planar antennas, low-temperature co-fired ceramic (LTCC)-based RF components and modules, packaging effects of microwave circuits, vehicle collision warning radars, and communications in intelligent transportation systems (ITSs).

Dr. Chung was the treasurer of IEEE Taipei Section (2001–2003) and the chairman of IEEE Microwave Theory and Techniques Society (IEEE MTT-S) Taipei Chapter (2005–2007). He was the recipient of the Outstanding Engineering Professor Award of the Chinese Institute of Engineers (2012), the Outstanding Electrical Engineering Professor Award of the Chinese Institute of Electrical Engineering (2006), and the Teaching Excellence Award of National Chiao Tung University (2005).